Analysis of the seasonal variations of equatorial plasma bubble occurrence observed from Haleakala, Hawaii

J. J. Makela, B. M. Ledvina, M. C. Kelley, P. M. Kintner

Annales Geophysicae (2004) 22: 3109–3121
SRef-ID: 1432-0576/ag/2004-22-3109

Annales Geophysicae

Analysis of the seasonal variations of equatorial plasma bubble occurrence observed from Haleakala, Hawaii

J. J. Makela[1], **B. M. Ledvina**[2], **M. C. Kelley**[2], **and P. M. Kintner**[2]

[1]E.O. Hulburt Center for Space Research, Code 7607, Naval Research Lab., Washington, District of Columbia 20375, USA
[2]School of Electrical and Computer Engineering, Cornell University, Ithaca, New York, 14853, USA

Received: 20 August 2003 – Revised: 20 January 2004 – Accepted: 25 February 2004 – Published: 23 September 2004

Part of Special Issue "Equatorial and low latitude aeronomy"

Abstract. Over 300 nights of airglow and GPS scintillation data collected between January 2002 and August 2003 (a period near solar maximum) from the Haleakala Volcano, Hawaii are analyzed to obtain the seasonal trends for the occurrence of equatorial plasma bubbles in the Pacific sector (203° E). A maximum probability for bubble development is seen in the data in April (45%) and September (83%). A broad maximum of occurrence is seen in the data from June to October (62%). Many of the bubbles observed from June through August occur later in the evening, and, as seen in the optical data, tend to be "fossilized." This suggests that the active growth region during these months is to the west of the observing location. These seasonal trends are consistent with previous data sets obtained both from other ground-based and satellite studies of the occurrence of equatorial bubbles in the Pacific sector. However, our data suggests a much greater probability of bubble occurrence than is seen in other data sets, with bubbles observed on over 40% of the nights studied.

Key words. Ionosphere (equatorial ionosphere; ionospheric irregularities; instruments and techniques)

1 Introduction

The low-latitude irregularity process caused by the generalized Rayleigh-Taylor instability, often referred to as equatorial spread-F (ESF), has been the subject of countless studies since its first observation in the 1930s by Booker and Wells (1938). This instability manifests itself as a bubble, or more properly, a wedge, of depleted plasma that bursts through the F peak into the topside ionosphere. The associated turbulence spans many decades of wavelength and can have severe effects on communication and navigation systems that rely on transionospheric propagation, such as the Global Positioning System (e.g. Kintner et al., 2001; Kelley et al., 2002). As such, understanding the occurrence statistics and underlying physical mechanisms for bubble development has been a major topic of study, with the eventual goal being the ability to predict when and where a bubble will form.

To this end, an extensive database of the seasonality of equatorial plasma bubbles across all longitudes needs to be developed. Much work has been done already, and numerous data sets exist for many locations based on observations from various instruments (we point the reader to the most recent reviews of the topic by Aarons (1993) and Abdu (2001), and references therein for a more thorough discussion of the different observing techniques and databases available). In addition to the radio techniques used to study the scintillations associated with ESF, many optical studies have been performed in recent years to image the equatorial plasma bubbles that are associated with the Rayleigh-Taylor instability (e.g. Sahai et al., 2000; Martinis et al., 2003; Pimenta et al., 2003b; Mukherjee, 2003).

One of the main features that becomes evident from the study of this large body of work is that different longitude sectors have different "spread-F seasons". A general understanding of this seasonality and longitudinal dependence has been developed, most notably by Tsunoda (1985) and Maruyama and Matuura (1984). Tsunoda (1985) described the pattern of irregularity occurrence based on the alignment of the solar terminator and the geomagnetic flux tubes. Based upon a compilation of previous radio observations, he found that the irregularities were most prevalent near times of the "sunset nodes" (when the conjugate E regions on a magnetic flux tube enter darkness at the same time), which is the time when the E-region Pedersen conductivity gradient is the largest. Maruyama and Matuura (1984) presented a framework in which the transequatorial neutral wind acted as an inhibitor to the growth of the Rayleigh-Taylor instability process. This was based upon topside sounding measurements made by the Ionosphere Sounding Satellite b over a two-year period. They found that irregularities were most

Correspondence to: J. J. Makela
(jmakela@ssd5.nrl.navy.mil)

Table 1. Description of the Cornell All-Sky Imager (CASI) and Cornell Narrow-Field Imager (CNFI) used in this study.

	CASI	**CNFI**
Camera Type:	Princeton Instruments	Photometrics 300
Field-of-view:	180°	47°
Center look-direction:	Zenith	el: 17.9° az: 188.0°
Filters:	557.7 nm	557.7 nm
	630.0 nm	630.0 nm
	777.4 nm	777.4 nm
	Background (541.0 nm)	Background (541.0 nm)
	Sodium (589.0 nm)	

prevalent when the distribution of electron density around the magnetic equator was symmetric, while an asymmetry in the distribution was associated with a lack of irregularities. They concluded that the absence of a transequatorial thermospheric wind in the magnetic meridian was a necessary condition for the growth of equatorial plasma bubbles. Although an understanding of the gross characteristics of the occurrence of equatorial plasma bubbles has thus been developed, the questions of day-to-day variability and forecasting of these irregularities remain unanswered and are currently the focus of much research (Basu et al., 2002).

We report here on a new data set that is being compiled for the Pacific sector using instrumentation atop the Haleakala Volcano on Maui, Hawaii. It is our hope that this data set (which continues to grow) will provide new insights into the seeding, development, and persistence of equatorial plasma bubbles, both on its own and when combined with other ground- and space-based observations (e.g. Kelley et al., 2003). We will show that our observations from Hawaii agree with the gross characteristics expected for the Pacific region based on previous studies from locations further to the west in the Pacific sector (the closest location of previous long-term studies is Suva, Fiji (Buonsanto et al., 1987), which is over 20° to the west of Hawaii). However, we also show that our high-temporal resolution optical studies reveal subtleties not accounted for in the frameworks of Tsunoda (1985) and Maruyama and Matuura (1984). Specifically, the optical observations of equatorial bubbles allows for the determination of whether bubbles are actively growing, or "fossilized" remnants of bubbles that developed to the west and have drifted into the field-of-view of the imager, providing a more refined estimate of the growth regions of these irregularities.

In this paper, we first describe the instrumentation used to obtain the data on the occurrence of equatorial plasma bubbles. Next, we present the data obtained over one-and-a-half years worth of observing time, from January 2002 until August 2003. We describe the data and present our interpretations. This is followed by comparisons to other data sets that have been compiled for the Pacific sector, both from instruments on the ground (e.g. photometers and radio receivers) and onboard satellites (e.g. ion drift meters). We conclude with a discussion of other useful parameters that can be obtained from this data set, as well as future directions that should be taken.

2 Instrumentation

All of the instrumentation used in this study is located atop the Haleakala Volcano on the island of Maui, Hawaii (geographic: 20.7° N, 203.7° E; geomagnetic: 21.3° N, 271.4° E) at the Maui Space Surveillance Site (MSSS) as part of the NSF and AFOSR sponsored Maui Middle Atmosphere and Lower Thermosphere (Maui-MALT) initiative. The initial installation was performed in December of 2001, with each system coming online for routine observations at the beginning of 2002. The systems described below run completely autonomously, only requiring user intervention in the case of a system crash or hardware failure. The various components have been briefly described in previous publications, but we include the pertinent descriptions here for completeness.

The Haleakala Volcano is an excellent observing site for this study because it lies at a magnetic latitude that allows for observing the longitudinal and vertical structure of equatorial plasma bubbles (EPB) associated with equatorial spread-F (ESF) (Tinsley, 1982). EPBs are generated close to the magnetic equator but, due to the high conductivity along the magnetic field lines, the generated electric fields are efficiently mapped to poleward latitudes. These electric fields then perturb the local ionosphere creating the structure that can be observed at equatorial and mid-latitude stations in either hemisphere, as shown in Otsuka et al. (2002). Optical observations of these structures can be mapped back along the magnetic field lines to show the vertical and longitudinal structure of the original bubble. Tinsley (1982) showed that the ideal latitude for making these sorts of observations was in a narrow band about 6° wide centered on $\pm 20°$ magnetic latitude.

2.1 Imaging systems

Among the many different imaging systems in the Maui-MALT initiative, two separate airglow systems have been deployed atop the Haleakala Volcano that include filters for studying the ionosphere. These are the Cornell All-Sky Im-

ager (CASI) and the Cornell Narrow-Field Imager (CNFI). Both CASI and CNFI use scientific-grade, back-illuminated CCDs fronted by telecentric optics, a filter-wheel, and a primary optics lens to capture images of specific emissions in the Earth's mesosphere and ionosphere. Both CCDs have 1024×1024 pixels, which are binned on-chip by a factor of 2 to reduce the effects of readout noise, resulting in image sizes of 512×512. The CCDs are cooled to approximately -40° C to minimize the noise in the images. The filter-wheel houses narrow-band interference filters that determine the wavelength (and thus the emission) being imaged. The exposure time for each filter is 90 seconds. The imagers are controlled by separate PCs using a program developed at Cornell University. This program determines when the imager will take images (based on the location of the Moon and Sun), as well as the sequencing of the filters. When desired, different filter sequences can be used, although as a default a single image is obtained from each filter per cycle. The specifics of each system, including the field-of-view and the filters used, are given in Table 1. Two of these filters, at 630.0 nm and 777.4 nm, are of primary interest here, as the emissions they isolate are good tracers of the dynamics of the ionosphere. The peak intensity of the 557.7-nm emission is at 95 km (Taylor et al., 1995), although at times a significant proportion can come from the ionosphere (e.g. Kelley et al., 2002). The peak in the sodium emission occurs slightly lower than this (at approximately 89 km). These two filters are included to study the mesosphere and, as we are interested in the ionosphere in this paper, will be ignored here.

The 777.4-nm emission is a result of the radiative recombination of O^+ (Tinsley et al., 1973). At F-region heights the ionosphere is dominated by O^+ ions, and the volume emission rate for this reaction is proportional to the square of the electron density. The peak in the 777.4-nm emission occurs at the F peak, with typical values for low- and mid-latitudes being around 350 km. If we assume that the electron density profile can be approximated by a Chapman profile, the observed quantity becomes proportional to the square of the peak electron density (e.g. Sahai et al., 1981a; Makela et al., 2001). Thus, optical observations of the 777.4-nm emission can be used to study the dynamics that affect the electron content of the ionosphere.

The emission at 630.0-nm is a result of the dissociative recombination of O_2^+ (Link and Cogger, 1988) and has been used extensively by the ionospheric community as a tracer for the dynamics of the ionosphere (e.g. Tinsley and Bittencourt, 1975; Sahai et al., 1981b; Mendillo et al., 1997; Sahai et al., 2000; Makela et al., 2001; Pimenta et al., 2003a). The volume emission rate for this reaction has a strong dependence on both the electron density and the neutral O_2 density. This dual-dependence slightly complicates the interpretation of images of the 630.0-nm emission, as a brightening (dimming) of the emission could be due to either an increase (decrease) in electron density or the lowering (raising) of the F layer as a whole. However, as described in Makela et al. (2001), when used in conjunction with the 777.4-nm emission, this dual-dependence can yield information on the height of the F layer, resulting in two-dimensional maps of the height and density of the ionosphere. The peak in the 630.0-nm emission occurs roughly one scale height below the F peak, with typical values for low- and mid-latitudes being 250–300 km. Unfortunately, images of the 630.0-nm emission tend to be a bit blurred, as seen below, due to the long lifetime of the $O(^1D)$ state (110 s) that leads to the emission of the 630.0-nm photon. This blurring seen in the 630.0-nm images in comparison to the 777.4-nm images has been shown in Abalde et al. (2001).

The fields-of-view of the two imagers, assuming emission heights of 350 km for the 777.4-nm emission and 300 km for the 630.0-nm emission, are shown in Figure 1a. A cutoff-angle of 30° is used for CASI, as near-field obstructions tend to limit the useful field-of-view to this value. CNFI is pointed with a central look-angle of 17.9° elevation and 188.0° azimuth. The azimuthal direction is chosen so that it aligns with the magnetic meridian, while the elevation is chosen so that the central look-angles are tangent to the magnetic field lines at 350 km. As can be seen, the two fields-of-view overlap slightly, and when combined cover a very extensive region of the ionosphere. In Fig. 1b we show the fields-of-view of the two cameras mapped along the magnetic field lines to the magnetic equator. The combined fields-of-view of the two cameras effectively probe from 350 km to well over 1500 km over an 18° longitudinal range.

Sample images from CASI and CNFI are shown in Fig. 2. The top panels show a very extensive depleted region associated with ESF captured using CASI. The bottom panels show the same structure, but observed using CNFI. Images taken with the 630.0-nm filter are presented on the left, while those taken with the 777.4-nm filter are on the right. Notice the relative blurring of the 630.0-nm images when compared to the 777.4-nm images. These images can be processed as described above and projected either to an assumed emission altitude (as in Figure 1a) or to the magnetic equator (as in Fig. 1b), to study the spatial characteristics of these depletions.

Tinsley (1982) showed that the resolution of the type of viewing scheme employed here is best at look-angles that are tangent to the magnetic field lines at F-peak heights and degrades as the look-angle intersects multiple field lines. This is evident in the images captured by CASI and CNFI as structures drift through the fields-of-view. Figure 2 shows an example of this effect, where small-scale structure can be seen in the center of the CNFI 777.4-nm image (bottom-right) but not near the edges of the same image. Small-scale structure, on the order of a few kilometers in the equatorial plane, can be seen when the viewing geometry is optimal, whereas small-scale structure becomes blurred when not in this optimal geometry. It is important to note that this is different than the resolution of the imaging system. It is instead a limiting factor based on the observing geometry.

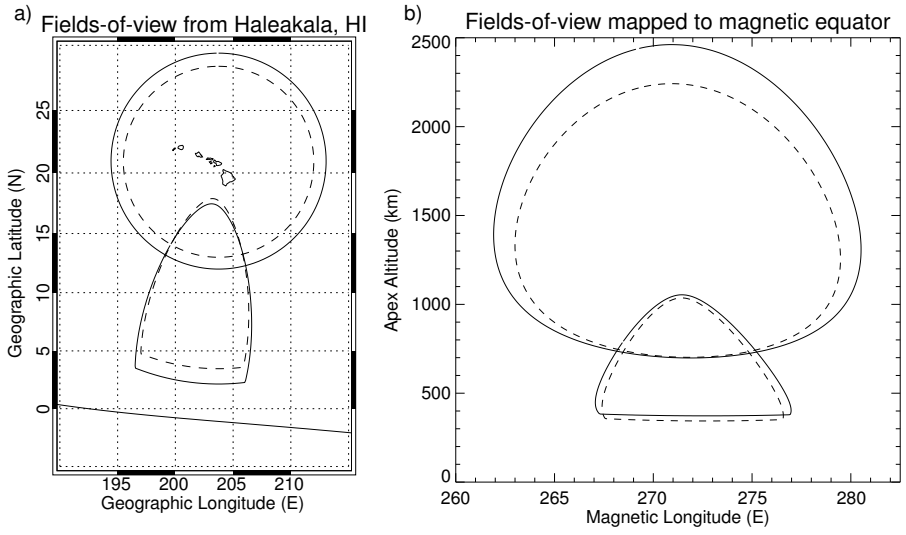

Fig. 1. (a) Fields-of-view for CASI (circles) and CNFI (arch-shape) for 350-km (solid line) and 300-km (dashed line) emission layers. The bold line near the bottom of the figure is the magnetic equator. **(b)** The projected fields-of-view of the two cameras at the magnetic equator.

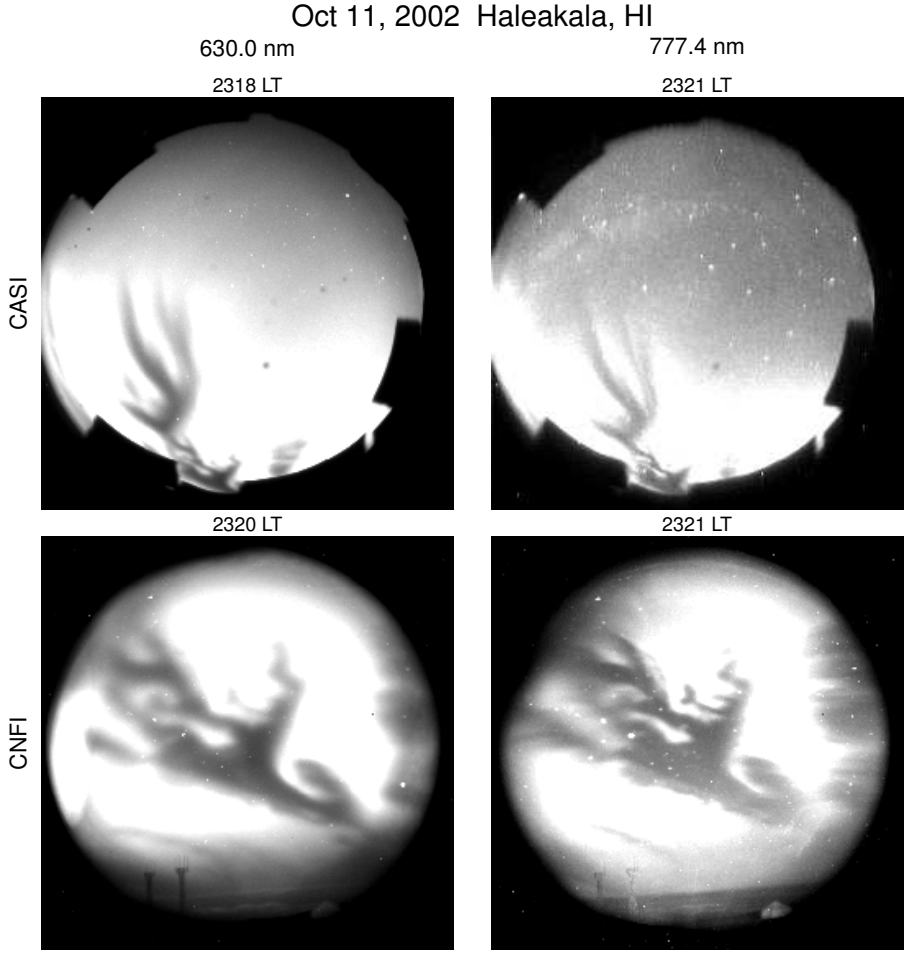

Fig. 2. Example images of equatorial plasma bubbles captured with CASI (top images) and CNFI (bottom images) using the 630.0-nm filter (left images) and the 777.4-nm filter (right images). In these images, north is at the top of each image and west is to the left.

2.2 GPS receivers

In addition to the two airglow systems described above, we have also placed two Global Positioning System (GPS) receivers at the site. The first is a single-frequency (L1 at 1.5754 GHz) GPS receiver developed at Cornell University to record the signal power of the received GPS signals at a 50-Hz sampling rate (Beach and Kintner, 2001). From the measurements of the signal power, the S_4 index can be calculated. The S_4 index is defined as the unity normalized standard deviation of the received signal power and is given by:

$$S_4 = \sqrt{\frac{\langle I^2 \rangle - \langle I \rangle^2}{\langle I \rangle^2}}, \quad (1)$$

where I is the signal intensity and the brackets indicate an ensemble average (Yeh and Liu, 1982). The S_4 index was originally introduced to characterize the strength of fluctuations about the mean of a received signal. The fluctuations are caused by wave diffraction due to the presence of irregularities. These fluctuations are, under weak scintillation theory, physically dependent on the root mean square of the plasma density fluctuations, ΔN, and the square root of the thickness of the scattering medium. The S_4 index, however, was not designed to allow for significant changes in the mean of the signal intensity. With the GPS, the received signal intensity is a function of satellite elevation, where the signal is weakest at low elevations. This effect can cause S_4 indices of low elevation satellites to be larger than physically expected. Indeed, this is the case in our data, as low elevation satellites exhibit on average slightly higher S_4 indices (0.2) than high elevation satellites (0.1). However, the values chosen in this study to indicate moderate (0.5) and severe (0.75) scintillations are significantly above these elevation-dependent quiet time levels. Furthermore, the moderate and severe scintillations do not only occur at low elevations, but often occur at higher elevations, with some close to zenith. Kelley et al. (2002) have shown that the locations of the severe scintillations correspond with the depleted regions in the optical observations. This gives us confidence that the GPS-L1 scintillations we are presenting here are truly associated with EPBs and are not just an artifact of the satellite-receiver geometries.

In general, if the signal from a GPS satellite passes through a disturbed region of the ionosphere, such as an EPB, it will scintillate. This is seen as an increase in the S_4 index, as defined above. Thus, the scintillation receiver can quantify the severity of any disturbance that passes over Hawaii. It is important to note that the scale size of the irregularities that cause the fluctuations of a given radio signal is the Fresnel radius, which for the GPS-L1 frequency is about 400 m. For this reason, the S_4 index at two different frequencies will not be the same, with that for lower-frequency signals typically higher than for higher-frequency signals. The advantage of this type of instrument over the airglow systems described above is that it is not limited by clouds or the Moon. However, it is limited by the number and locations of the GPS satellites. Typically for the Haleakala site there are more than six satellites distributed about the sky for making scintillation observations at any given time.

The second GPS system that we use is a NovAtel dual-frequency (L1 at 1.5754 GHz and L2 at 1.2276 GHz) receiver. This receiver is used to determine the total electron content (TEC) between the receiver and the GPS satellites. The TEC has been shown to correlate well with airglow images (e.g. Weber et al., 1996; Garcia et al., 2000; Kelley et al., 2000). Thus, the information on TEC gained from the dual-frequency receiver could be used to quantify the electron depletion seen inside of the equatorial plasma bubbles. However, Kelley et al. (2002) showed that for severely scintillated GPS signals, a loss-of-sync could occur for the NovAtel receiver, causing it to lose a lock on the GPS-L2 frequency, making TEC estimates impossible. The TEC information can still be used, though, to provide estimates of the electron content in the pre-sunset hours, which is thought to be the most important time in determining whether or not equatorial bubbles will develop. However, this use of the GPS-derived TEC falls out of the scope of this paper.

3 Data description

The systems described above were installed at the end of 2001 and began operating on a routine basis in January 2002. The data collected by the camera systems are limited to clear nights. Collection begins when the center of the Sun's disk is 18° below the horizon and ends when the Sun reaches this angle again. In addition, the all-sky camera is limited to times when the Moon is below the horizon. CNFI was operated in the same mode (not taking data when the Moon was above the horizon) until the end of February, 2002 when it was decided that the Moon, as observed from Hawaii, rises to a sufficiently high elevation angle as to not pose a significant concern to this imager. However, it should be noted that additional light contamination occurs at times when the Moon is up and CNFI is collecting data. Yet it can still be determined whether or not an EPB is present in these images, and so operating the narrow-field camera in this mode allows for significantly more data to be collected. For this reason, after 1 March 2002, CNFI collected data each night from sunset to sunrise, while CASI collected data only when both the Sun and Moon were below the horizon.

The observation statistics are shown for CNFI in Fig. 3 and for CASI in Fig. 4. In these figures the x axis shows the day of year and the y axis shows the local time. The data have been binned into half-hour increments for the purpose of these figures, although the temporal resolution of the data is closer to eight minutes. In Table 2, we provide a breakdown by month of the number of nights, with a minimum of one hour of observations during clear skies and those with observed EPBs. This is provided to make a comparison to other studies, which typically present data in monthly bins, a more straightforward approach.

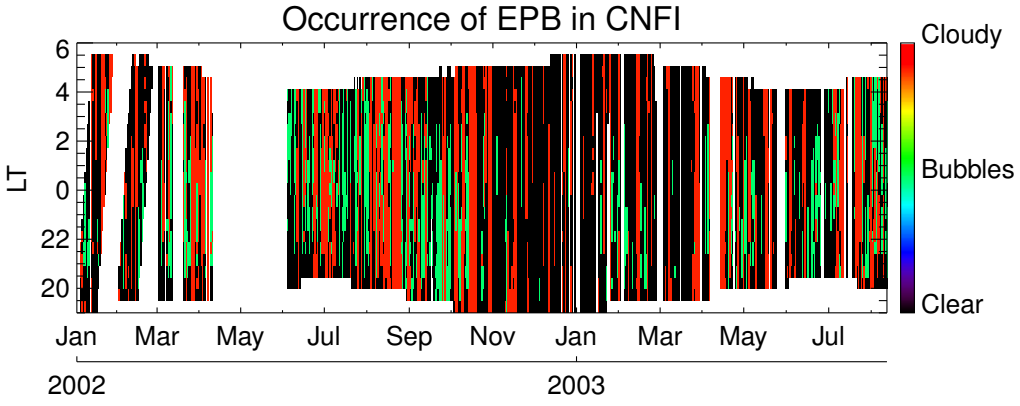

Fig. 3. Observations made by CNFI. Black represents times of clear skies and no observed EPB. Green represents times of observed EPB. Red represents time when observations were made but, due to clouds or light contamination, the data was unusable. White represents times when the camera was not operating, either due to maintenance or unfavorable Moon conditions. The tick mark above the month corresponds to the first day of that month.

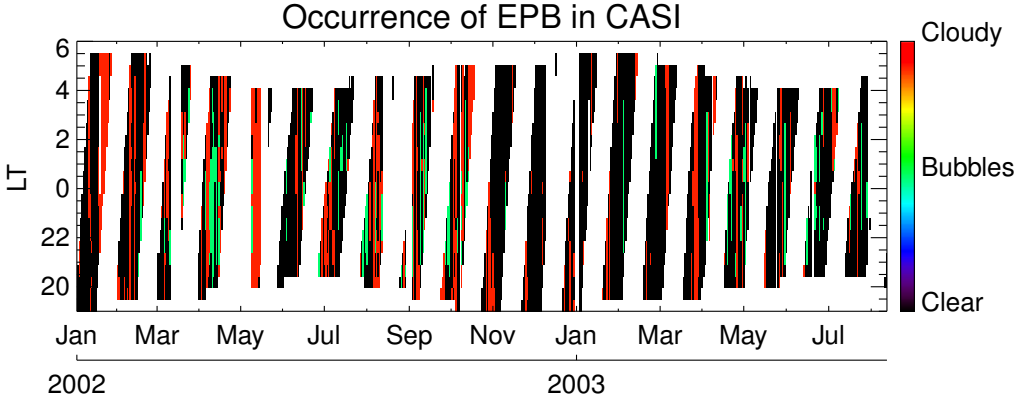

Fig. 4. Same as Fig. 3, but for CASI.

Examining Fig. 3 and Table 2 in more detail we see that a substantial amount of data was collected during this study. The diagonal data gaps (white strips) seen at the end of January and February are from when CNFI was not taking data due to unfavorable Moon conditions. The transition to the data taking mode that ignored the location of the Moon is easily seen on 1 March 2002 when a full night's worth of data was taken, even though the Moon was up (as seen in the previous night's lack of data). After this time there is only one other significant data gap, from 10 April to 2 June 2002, that was due to a shutter problem that required refurbishment of the camera. After this, CNFI ran at a very high duty cycle, with only a few isolated nights having no data collected, usually due to a minor computer problem. Overall, from 1 January 2002 through 15 August 2003, 480 nights of observations were made. Of these nights, 408 were predominately clear (defined as having minimal cloud cover in at least one hour's worth of data) and 184 exhibited plasma bubbles. For the images collected by CNFI, any images that showed vertical depleted regions (when projected to the equatorial plane) were deemed to be indicative of an EPB. No attempt was made to distinguish whether or not the bubbles penetrated through the F layer to reach the topside, or if they remained on the bottomside.

Turning to Fig. 4 we can easily see the amount of observing time that is lost due to the Moon. During the period being considered here, CASI made observations on 440 nights, 376 of which were predominately clear while 64 exhibited plasma bubbles. For the images collected by CASI, only depleted regions that extended to magnetic latitudes corresponding to equatorial altitudes above 1000 km were considered. In this sense, the data of Fig. 4 can be viewed as nights of towering plumes, all of which have broken through the F layer to the topside, in some cases extending to latitudes corresponding to over 1500 km.

It should be noted that a careful examination of Figs. 3 and 4 will reveal periods when the CASI data was deemed "cloudy" while the CNFI data was deemed "clear", or vice versa. The criterion for marking an image as "cloudy" was if a majority of the image was obscured by clouds upon visual inspection. As CNFI is observing a small region of the sky along the horizon and CASI is observing the entire overhead

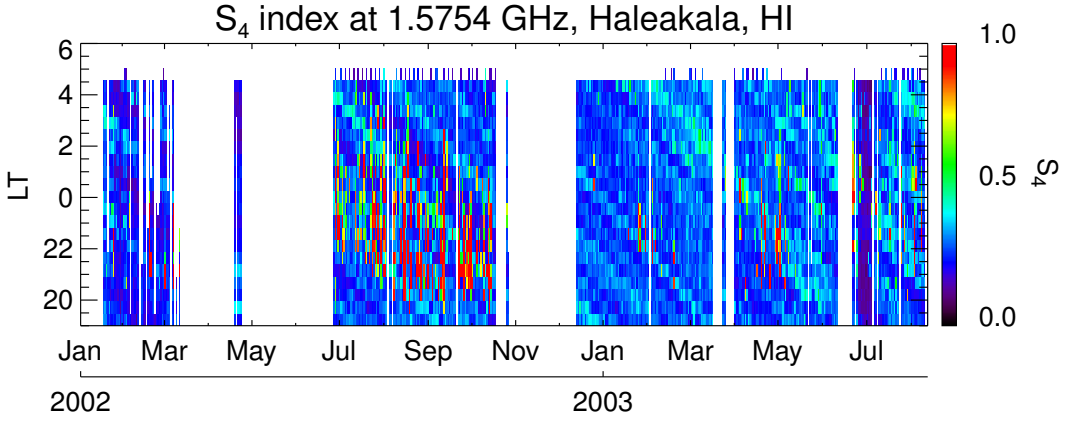

Fig. 5. S_4 index measured by the GPS-L1 scintillation monitor. The diagonal lines that can be seen in the data are an artefact caused by multipath and the gradually changing orbits of the GPS satellites.

Table 2. Breakdown by month of when observations were made and when EPBs were observed for the instrumentation used in this paper. For the two imagers, the data is presented as "number of nights with clear observations (number of nights with EPBs observed)". For the GPS receiver, the data is presented as "number of nights with GPS observations (number of nights with $S_4>0.75$)".

Month	CNFI	CASI	GPS
January	43(14)	38(0)	46(5)
February	48(15)	44(4)	52(6)
March	39(14)	39(5)	30(3)
April	21(11)	39(13)	33(8)
May	21(8)	31(4)	30(7)
June	49(29)	46(12)	23(5)
July	50(32)	47(11)	59(25)
August	33(22)	16(6)	43(22)
September	27(22)	17(7)	29(18)
October	20(11)	18(5)	20(12)
November	30(4)	23(1)	0(0)
December	27(2)	18(0)	18(1)
Total	408(184)	376(64)	383(112)

sky, it is plausible to have the majority of one imager's field-of-view contaminated by clouds while the other's field-of-view is predominately clear. For example, low-lying clouds along the southern horizon would completely fill CNFI's field-of-view, but only be seen in a small portion of CASI's field-of-view.

Unlike the imagers, the GPS-L1 scintillation receiver is not limited to making observations during the night when it is clear. The receiver was setup to make 50-Hz measurements of the GPS signal power received from each satellite in view. The S_4 index at 1.5754 GHz as defined in (1) was calculated for each satellite. In Fig. 5 we have plotted the maximum S_4 index measured for all satellites in view during 30-minute intervals. We have limited the plot to night-time (18:00–06:00 LT), as this is the time period of interest in this paper. There are several large data gaps in the GPS data caused by a problem with the GPS receiving antenna that prohibited data collection. For this study, 383 nights of scintillation data are used, 112 of which exhibit a maximum $S_4>0.75$.

4 Seasonal statistics of equatorial plasma bubbles

As a way to make sense of the large quantity of data collected by these systems, we have calculated the percentage of nights within a $\pm$10-day window for each half-hour bin in which there were observations (camera operating and no clouds or GPS receiver operating) and bubbles or scintillations were observed. This was done for every day and every 30-min bin for the data shown in Figs. 3, 4, and 5.

The statistics thus compiled for CNFI are presented in Fig. 6. Clear maxima can be seen to occur during the beginning of April 2002, at the end of September 2002, and late April 2003. The beginning of another maximum is alluded to at the end of the presented data in mid-August 2003. The April 2002 maximum should be viewed with some skepticism, however, since the number of valid data points within the 20-day window is severely limited due to the data gap that occurs in mid-April and the number of cloudy nights. This skepticism is confirmed by the 2003 data that shows a build-up of activity beginning later in April, when no data was being collected in 2002 due to hardware problems, as discussed above. The September equinoctial period in 2002, on the other hand, was during a time of relative clear skies and robust imager operation and thus we have more confidence in it. Besides the two near-equinoctial maxima, the other striking feature of Fig. 6 is the relatively common (>50%) occurrence of ESF in the late evening to early morning (22:00–04:00 LT), from June to August. This will be discussed in more detail below. The activity in February 2003 occurred during a period of geomagnetic activity, which can

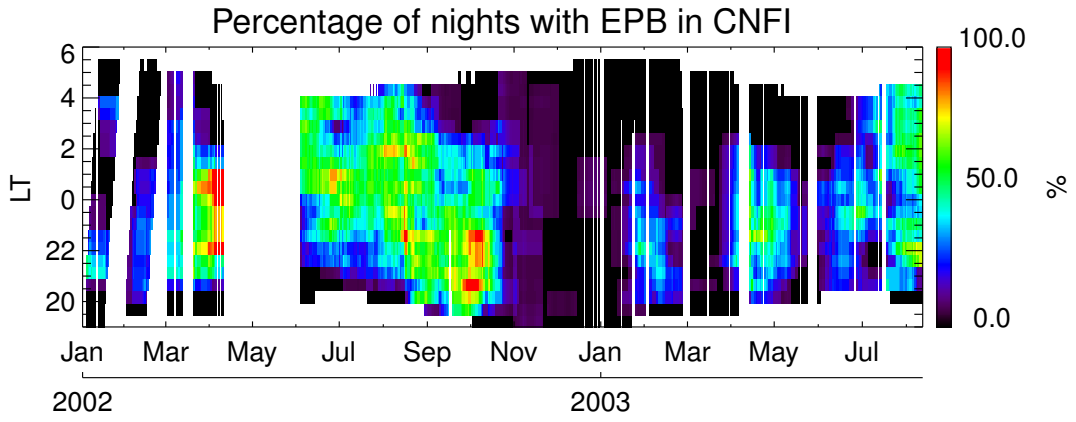

Fig. 6. EPB statistics using data collected by CNFI. The percentages were calculated for a 20-day window centered on each day for each half-hour bin.

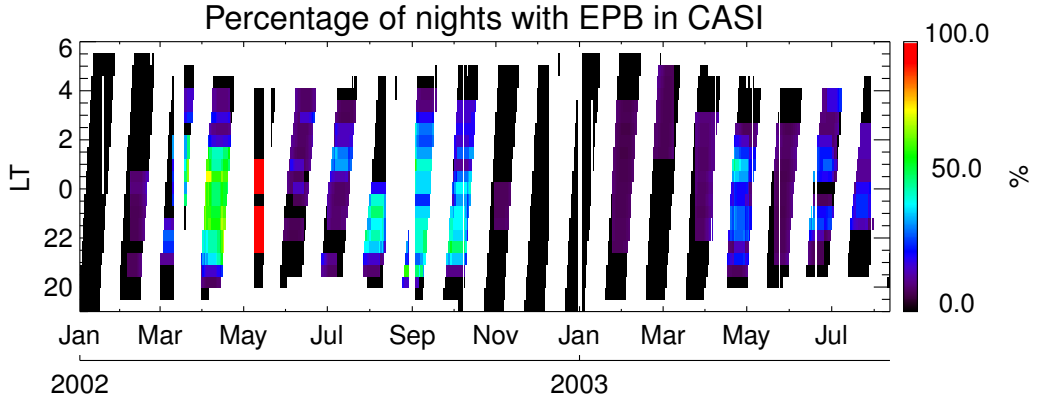

Fig. 7. Same as Figure 6, but for CASI.

have the effect of increasing irregularity development (Hysell and Burcham, 2002).

Figure 7 shows the statistics compiled for CASI. Again, maxima in the occurrence of EPBs are seen at the beginning of April and in September. As discussed above, the criterion for determining the existence of an EPB in the CASI data was that the depleted regions reach a latitude corresponding to an equatorial altitude over 1000 km. This explains why the percent occurrence is much lower in Fig. 7 than in Fig. 6. It is evident that the EPBs that occurred from June to August, as seen in the CNFI data, do not always reach high altitudes. In addition, the all-sky data occurrence rate is slightly delayed in local time relative to the CNFI rate, most likely due to the finite development time required for the bubbles to reach high altitudes.

In Fig. 8 we present the statistics compiled from the GPS-L1 scintillation data. Unfortunately, no data was collected during April–May 2002, but an increase in the occurrence of scintillations is seen in April–May 2003. During the September–October 2002 period, a maximum is seen to occur at the end of September through the beginning of October. The scintillation activity also develops at a slightly later local time than the CNFI data indicate. As with the CASI data, the GPS data is most sensitive to plumes that reach to a high equatorial altitude. However, it should be noted that large scintillations can and do occur at low elevation angles along southern look directions, corresponding to equatorial heights below 1000 km.

5 Discussion

From the data presented in Figs. 6 and 7 we see a clear tendency for the occurrence of equatorial plasma bubbles at Hawaiian longitudes during the near-equinoctial periods (mid-April until mid-May and mid-August until mid-October). It is during these periods that bubbles are often seen immediately after sunset. In fact, on most of these nights the vertical development of the plumes is seen, during which the depletions burst through the F layer and bifurcate multiple times, as seen in the numerical simulations of Zalesak et al. (1982).

This trend of high bubble activity immediately following sunset during the near-equinoctial periods is supported by the GPS data presented in Figure 8, where strong GPS scintilla-

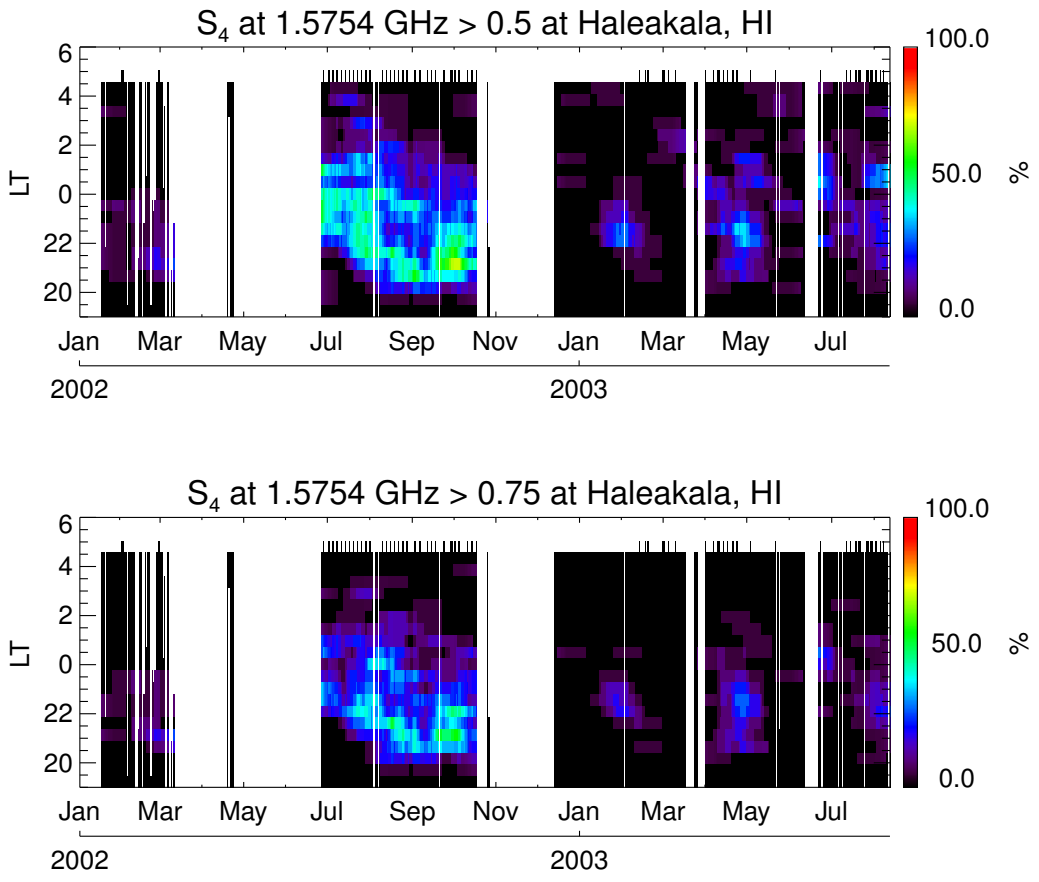

Fig. 8. Percentage of nights in a 20-day window on which the S_4 index at the GPS-L1 frequency exceeded 0.5**(a)** and 0.75**(b)**.

tions are seen to begin shortly after sunset, coincident with the observations of airglow depletions. Indeed, Kelley et al. (2002) showed that the regions of large S_4 indices at the GPS-L1 frequency corresponded to the regions of depleted electron density. This was done by mapping the GPS satellite ionospheric pierce points onto images taken at 777.4 nm.

In contrast to the active development seen in the near-equinoctial months, the depleted regions seen in the imager data from June through August drift through the fields-of-view of both imagers fully developed. They also tend to occur later in the evening with the majority appearing after 22:00 LT. As they drift through the region, they still affect the GPS scintillation monitor, which measures large S_4 indices for the satellites whose satellite-to-receiver look angles pass through the depletion (see Kelley et al. (2002) for an example).

These two trends are shown in Fig. 9. In the top panel we have plotted the percent of nights in each month when EPBs or intense scintillations ($S_4 > 0.75$) were observed between 19:30 and 21:30 LT. This is the period immediately after local sunset, indicating that the development region for these bubbles lies close to the Hawaiian longitude. In the bottom panel we have plotted the percentage of nights for each month when EPBs were observed after 22:00 LT. As seen in the imager data, these bubbles tend to drift into the field-of-view fully developed, suggesting that the seeding region is to the west of Hawaii. Comparing Figs. 9a and 9b, it is clear that the months of April and September are relative maxima for the generation of equatorial plasma bubbles in this region of the Pacific. From June to August, we are observing plumes that originate to the west and, due to the eastward drift typical of EPBs, pass by Hawaii later in the evening. As shown in Makela and Kelley (2003), the images taken with CNFI can be used to make an estimate of when and where these plumes developed. Alternately, their technique can also be used to make a prediction as to when plumes seen at Hawaii will affect locations to the east. For the June to August data presented here, the bubbles are observed to drift into the field-of-view of the cameras beginning approximately two-and-one-half hours after local sunset. Assuming a typical eastward drift speed of 100 m/s, this suggests that the bubbles developed approximately 900 km to the west of Hawaii. Similarly, the bubbles that are seen close to 04:00 LT would have developed approximately 3000 km to the west of Hawaii.

There is a significant drop off in the intensity of scintillations in the GPS data from 2002 to 2003, as seen in Fig. 8. This is due to the decreasing solar activity associated with approaching solar minimum conditions. Indeed, the average total electron content over Hawaii (not shown here) has de-

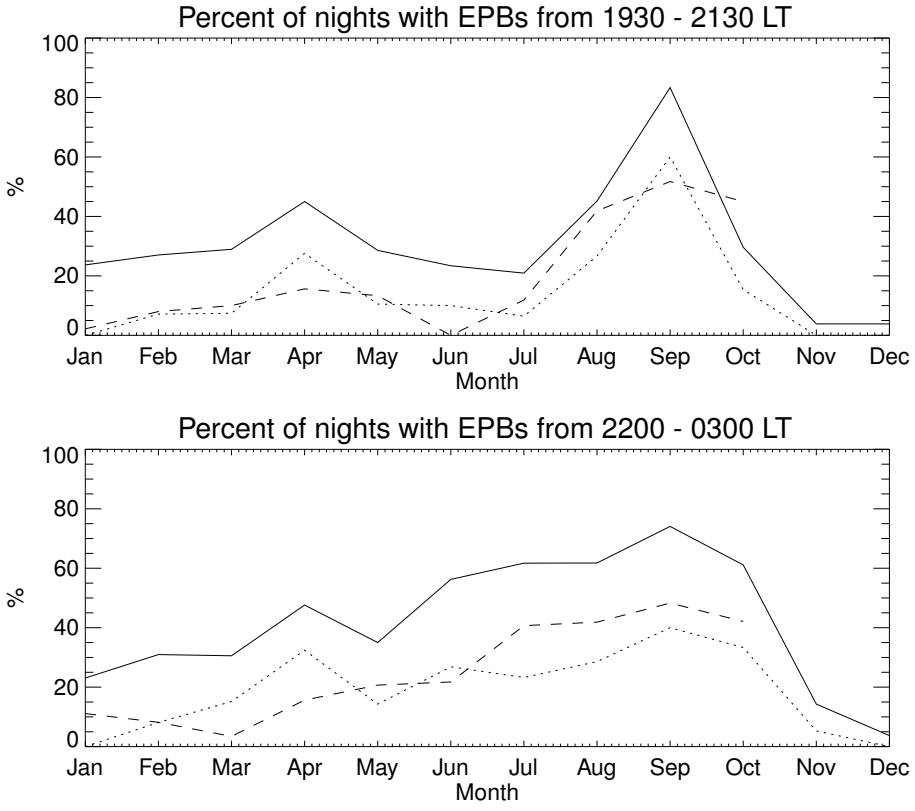

Fig. 9. (a) Percentage of nights with EPBs from 19:30–21:30 LT and (b) 22:00-03:00 LT for CNFI (solid line), CASI (dotted line), and the GPS-L1 scintillation monitor (S_4>0.75, dashed line).

creased significantly over the duration of this study. Furthermore, the scintillations seen after July 2003 disappear at an earlier time than they did during the corresponding period in 2002. However, as seen by comparing Figures 6 and 8, EPBs are still present after the scintillations have ceased. This suggests that the electron densities during this time are too low for significant scintillations to exist at 1.5754 GHz, even though the underlying EPB structure is still present.

6 Comparison to previous studies

Perhaps the study with the most significance relating to the occurrence pattern of equatorial plasma bubbles reported here is Kim et al. (2002). Using three years (April 1965 through October 1968, a time of minimum and increasing solar activity) of azimuth-scanning photometric observations of the 630.0-nm and 557.7-nm emissions taken from the Haleakala Volcano, these authors searched for evidence of depletions indicative of bubbles. Of the 161 nights with data, 16 were determined to have bubbles present. From the data presented in their Table 1, a maxima in September to October is evident, with an additional maximum, slightly lower in amplitude, in April.

Buonsanto et al. (1987) published results obtained at Suva, Fiji (geographic: −18.1°N, 178.4°E; geomagnetic: −25.7°N, 253.7°E) using over four years (September 1978 through March 1983, a time of increasing and maximum solar activity) of scintillation measurements at 4 GHz. These authors found a peak in the occurrence of 4-GHz scintillations from April until May and again from August until September. The occurrence rate was about 10% in both of these periods. A shallow minimum was found to occur from June to July. The data presented in this paper, as with the Kim et al. (2002) study, were only binned according to month, so we cannot determine if this shallow minimum is due to scintillations occurring later in the evening, as suggested by the data presented here. The other months showed negligible activity.

Further to the west and using signals transmitted from the Defense Nuclear Agency (DNA) Wideband Satellite from October 1976 through October 1977 (a period of solar minimum), Livingston (1980) showed scintillation data at multiple frequencies measured from Kwajalein, Marshall Islands (geographic: 9.25°N, 167.5°E; geomagnetic: 13.72°N, 237.83°E). This study reported peaks in scintillation activity in May and from July through August. Again, a shallow minimum was found in the northern summer months. For scintillations with S_4>0.6 at 413 MHz, the occurrence rate was found to be a bit higher than 10% in the April-May maximum and close to 15% in the July-August maximum. For the data presented at L-band frequencies (1.239 GHz), very few events were seen to have S_4>0.6, although peaks in the

occurrence of events with $S_4 > 0.2$ are seen in May and August.

All three of these ground-based studies agree fairly well with the observations presented here in that they show maxima occurring in April and late August to early September, although there seems to be a trend of increasing occurrence to the west of Hawaii during the northern summer months. However, the occurrence rate of EPBs in these previous studies is significantly lower (10%–15% during the September equinox) than what we have observed in this study (70% during the September equinox). Two of the studies (Livingston, 1980; Kim et al., 2002) use data collected during times of solar minimum. This could be the cause of the discrepancy in occurrence rates, as post-sunset EPBs reach higher altitudes during solar maximum periods (Hysell and Burcham, 2002). Thus, during solar minimum periods, bubbles may not reach altitudes high enough to affect the field lines observed from Hawaii or Fiji. In addition, as mentioned above, the irregularity amplitude of the scintillations is proportional to the mean electron density. Thus, during solar minimum conditions, when the electron density is decreased, we would not expect to see large S_4 values on transionospheric radio signals. In contrast to the Livingston (1980) and Kim et al. (2002) studies, the Buonsanto et al. (1987) study used data collected near solar maximum. However, their scintillation data was for a 4-GHz signal. Higher frequency signals are less susceptible to scintillations (see, for example, Fig. 2 of Livingston, 1980). This could explain why only 10% of the nights during the fall equinox in their study showed scintillation, even though it was at a time near solar maximum.

Other studies have been performed using "in-situ" data from instruments on board satellites. These studies can provide good global coverage of bubble occurrence, although caution must be used when trying to interpret these data. Depending on the orbit parameters of a satellite, different local times can be sampled across the globe or for a given site. As shown here, the occurrence of bubbles not only varies with season, but with local time. In addition, the altitude of the satellite must be taken into consideration, as one too high might miss developing or shorter bubbles. With this said, the results here compare favorably with typical satellite surveys.

McClure et al. (1998) studied the occurrence probability of equatorial F-region irregularities based on data collected from the ion drift meter on the AE-E satellite during the period of January 1978 through September 1980 (a period of increasing and maximum solar activity). The altitude of the satellite was increasing from 300 km to 475 km during this time, thus the satellite was low enough that the altitude of the satellite should not bias the results. They found the probability of having F-region irregularities maximized for the longitude of our observing station in the May-June-July period, with close to a 30% probability. A secondary maximum of about 25% probability occurs in the August-September-October period. The occurrence rate in the February-March-April period is about 15%, while the November-December-January period shows a rate of only 8%. Based on the results from our observations from Hawaii, the choices of three-month periods presented in the McClure et al. (1998) study may not be optimal for determining the "spread-F season" in the Pacific sector. However, it is interesting to note that their data show an increased probability of irregularities to the west of Hawaii during May-June-July, with a probability over 40% for 180° E geographic. This supports our assertion earlier that during this period, the main region of bubble development in the Pacific is to the west of Hawaii, explaining why we begin to see bubbles in our data later in the evening during the northern summer months than we do at the equinoxes.

The final study of comparison is that of Huang et al. (2001). These authors used data collected by the ion drift meter on board two DMSP satellites (F9 and F10) during 1989 and 1991 (both years close to solar maximum). Unlike the relatively low-flying AE-E satellite, the DMSP satellites orbit at ∼840 km, giving rise to the possibility that some bubbles might be missed in the Huang et al. (2001) data set. Thus, this data set is most comparable to the data presented here from CASI, for which we applied a minimum altitude of 1000 km for the bubbles. This is confirmed, as for each of the four periods studied in the McClure et al. (1998) study, the corresponding data from the Huang et al. (2001) study shows an occurrence rate for the Hawaiian sector that is lower than the CNFI or GPS derived data. The maximum probability for bubble encounters in the DMSP data is found to be during the August-September-October (20%) period, with lower probabilities in May-June-July (15%) and February-March-April (10%). A negligible probability of encounters was found during the November-December-January period. Again, evidence for an increasing number of bubble encounters to the west of Hawaii seen during May-June-July supports our assertion that the seeding region in the Pacific during the northern summer months lies to the west of Hawaii.

Huang et al. (2001) give an equation that represents the probability of encountering a bubble based on their data. Using this equation for the longitude of Haleakala, Hawaii gives a 7.1% probability of observing an EPB. By means of comparison, using only data collected by CASI in the 19:30 to 21:30 LT time frame (the local times used in the Huang et al. (2001) study), we find bubbles in 6.1% of our clear images. Using data from CNFI in the same way, we find a probability of 18.3%, a much higher probability that reflects the occurrence of plasma bubbles that do not reach altitudes greater than 1000 km. This just illustrates what was mentioned above; namely that statistical studies of equatorial plasma bubble occurrence using satellite data must be used carefully. Even bubbles that do not fully develop into towering plumes can still have a significant effect on transionospheric radio signals, albeit over a more limited range of latitudes.

Our observations from Hawaii agree with the broad understanding of the seasonal and longitudinal occurrence of equatorial plasma bubbles laid out in Tsunoda (1985) and Maruyama and Matuura (1984). The sunset nodes for the Hawaii longitude occur in mid-April and late August, which agrees with the relative maxima in the occurrence rate in de-

veloping bubbles, as shown in Fig. 9a. Similarly, we find an increased occurrence rate of bubbles in the northern summer months, which agrees with the findings of Maruyama and Matuura (1984). However, the high-temporal resolution of our observations reveal an interesting discrepancy with these studies during the months of June through August, when the development region is slightly to the west of the Hawaiian longitude, as discussed above. The typical difference between the first observation of a bubble and local sunset is approximately two-and-a-half hours. This puts the eastern edge of the development region about 8° to the west. This is not a significant distance, and the sunset nodes and declination (and thus the alignment of the transequatorial neutral wind and magnetic field) are virtually unchanged between Hawaii and this location. Thus, we conclude that some other mechanism must be considered, and may be related to various seeding mechanisms, as studied in McClure et al. (1998).

7 Conclusions

The results obtained from examining over 300 nights of data collected by airglow and GPS instrumentation located on the Haleakala Volcano on Maui, Hawaii are consistent with other ground- and satellite-based observations made in the Pacific sector. Relative maxima in the occurrence of bubbles are seen in April and September, with a shallow minimum centered during the northern summer months. A relative null is seen in the data during the northern winter months. A useful aspect of this data set is the ability to see the local time properties of the bubble occurrence. The events observed from June through August are seen to occur later in the evening, suggesting that the development region is in fact to the west of the observing site. This seems to be confirmed by satellite studies (McClure et al., 1998; Huang et al., 2001) that show a greater probability of encountering a bubble to the west of Hawaii during this time period. Furthermore, the bubbles seen in the airglow data collected for this period generally do not exhibit any vertical motion, indicating that they are "fossilized" and were formed earlier in the evening (and thus to the west). All of this suggests that there is some variable in the development of equatorial plasma bubbles heretofore unaccounted for, possibly a seeding mechanism as suggested by McClure et al. (1998), that can explain the shift in development regions slightly to the west of Hawaii from June to August. Unfortunately, this question cannot be satisfactorily answered using observations from a single location. This necessitates further studies using data from multiple locations closely spaced in longitude, to study the subtle changes in the seasonality and longitudinal occurrence of equatorial plasma bubbles not accounted for in the frameworks of Tsunoda (1985) and Maruyama and Matuura (1984).

A strong correlation is seen between the occurrence of towering plumes (as seen in the CASI data set) and strong scintillations of GPS signals at 1.5754 GHz. In fact, a one-to-one correlation is seen between GPS scintillations and the location of the bubbles when the two data sets are mapped to the same altitude (Kelley et al., 2002). Severe scintillations are seen inside of even the very old bubbles occurring later in the evening during 2002 when the electron densities are high enough. Early morning, intense scintillations are less common in the 2003 data due to the overall decrease in the total electron content associated with the approaching solar minimum.

Makela and Kelley (2003) have shown that the images obtained at this site can be used to form a single composite image. In doing so, the bubbles' eastward velocities can be obtained. In addition, an estimate of the formation time and longitude for each bubble can be made. More comparisons to satellite-based observations, such as that done by Kelley et al. (2003), need to be performed to verify these estimates.

As this data set continues to grow, we will be able to study the effects of the solar cycle on the occurrence rate and seasonality of EPBs in the Pacific sector. As suggested by Hysell and Burcham (2002), EPBs are seen earlier in the evening and at higher latitudes during solar maximum periods. They also tend to decay more rapidly during these periods. As we approach solar minimum, the data collected from Haleakala, Hawaii will be used to study these types of effects in more detail.

Acknowledgements. We thank the staff at the Maui Space Surveillance Site, especially R. Taft and S. Ah-You, for their extensive help in maintaining the instrumentation on the Haleakala Volcano. JJM is supported by a National Research Council Research Associateship Award at the Naval Research Laboratory. The work at Cornell University was supported by the Office of Naval Research under grants N00014-01-1-0702 and N00014-92-J-1822 as well as the Air Force Office of Scientific Research under grant F49620-01-1-0064.

Topical Editor M. Lester thanks P. Fagundes and another referee for their help in evaluating this paper.

References

Aarons, J.: The longitudinal morphology of equatorial F-layer irregularities relevant to their occurrence, Space Sci. Rev., 63, 209–243, 1993.

Abalde, J. R., Fagundes, P. R., Bittencourt, J. A., and Sahai, Y.: Observations of equatorial *F* region plasma bubbles using simultaneous OI 777.4 nm and OI 630.0 nm imaging: New results, J. Geophys. Res., 106, 30 331–30 336, 2001.

Abdu, M. A.: Outstanding problems in the equatorial ionosphere-thermosphere electrodynamics relevant to spread F, J. Atmos. Solar-Terr. Phys., 63, 869–884, 2001.

Basu, S., Groves, K. M., Basu, S., and Sultan, P. J.: Specification and forecasting of scintillations in communication/navigation links: current status and future plans, J. Atmos. Solar-Terr. Phys., 64, 1745–1754, 2002.

Beach, T. L. and Kintner, P. M.: Development and use of a GPS ionospheric scintillation monitor, IEEE T. Geodic. Remote., 39, 918–928, 2001.

Booker, H. G. and Wells, H. W.: Scatter of radio waves by the *F*-region of the ionosphere, Terr. Mag. and Atmos. Elec., 43, 249–256, 1938.

Buonsanto, M. J., Northcott, R. L., and Wright, R. W. H.: Rapid fluctuations in ionospheric Faraday-rotation angle and 4 GHz

amplitude scintillation observed at Suva, Fiji, Ann. Geophys., 5, 39–45, 1987.

Garcia, F. J., Kelley, M. C., Makela, J. J., and Huang, C.-S.: Airglow observations of mesoscale low-velocity traveling ionospheric disturbances at midlatitudes, J. Geophys. Res., 105, 18 407–18 415, 2000.

Huang, C. Y., Burke, W. J., Machuzak, J. S., Gentile, L. C., and Sultan, P. J.: DMSP observations of equatorial plasma bubbles in the topside ionosphere near solar maximum, J. Geophys. Res., 106, 8131–8142, 2001.

Hysell, D. L. and Burcham, J. D.: Long term studies of equatorial spread *F* using the JULIA radar at Jicamarca, J. Atmos. Solar-Terr. Phys., 64, 1531–1543, 2002.

Kelley, M. C., Garcia, F., Makela, J., Fan, T., Mak, E., Sia, C., and Alcocer, D.: Highly structured tropical airglow and TEC signatures during strong geomagnetic activity, Geophys. Res. Lett., 27, 467–468, 2000.

Kelley, M. C., Makela, J. J., Ledvina, B. M., and Kintner, P. M.: Observations of equatorial spread-F from Haleakala, Hawaii, Geophys. Res. Lett., 29, 2003, doi:10.1029/2002GL015 509, 2002.

Kelley, M. C., Makela, J. J., Paxton, L. J., Kamalabadi, F., Comberiate, J. M., and Kil, H.: The first coordinated ground- and space-based optical observations of equatorial plasma bubbles, Geophys. Res. Lett., 30, 1766, doi:10.1029/2003GL17 301, 2003.

Kim, Y. H., Hong, S. S., and Weinberg, J. L.: Equatorial spread *F* found in 5577 Å and 6300 Å airglow observations from Hawaii, J. Geophys. Res., 107, 1264, doi:10.1029/2001JA009 232, 2002.

Kintner, P. M., Kil, H., and Paula, E. D.: Fading time scales associated with GPS signals and potential consequences, Rad. Sci., 36, 731–743, 2001.

Link, R. and Cogger, L. L.: A reexamination of the O I 6300 Å nightglow, J. Geophys. Res., 93, 9883–9892, 1988.

Livingston, R. C.: Comparison of multifrequency equatorial scintillation - America and Pacific sectors, Rad. Sci., 15, 801–814, 1980.

Makela, J. J. and Kelley, M. C.: Field-aligned 777.4-nm composite airglow images of equatorial plasma depletions, Geophys. Res. Lett., 30, 1442, doi:10.1029/2003GL1017 106, 2003.

Makela, J. J., Kelley, M. C., González, S. A., Aponte, N. A., and McCoy, R. P.: Ionospheric topography maps using multiple-wavelength all-sky images, J. Geophys. Res., 106, 29 161–29 174, 2001.

Martinis, C., Eccles, J. V., Baumgardner, J., Manzano, J., and Mendillo, M.: Latitude dependence of zonal plasma drifts obtained from dual-site airglow observations, J. Geophys. Res., 108, 1129, doi:10.1029/2002JA009 462, 2003.

Maruyama, T. and Matuura, N.: Longitudinal variability of annual changes in activity of equatorial spread *F* and plasma bubbles, J. Geophys. Res., 89, 10 903–10 912, 1984.

McClure, J. P., Singh, S., Bamgboye, D. K., Johnson, F. S., and Kil, H.: Occurrence of equatorial *F* region irregularities: Evidence for tropospheric seeding, J. Geophys. Res., 103, 29 119–29 135, 1998.

Mendillo, M., Baumgardner, J., Nottingham, D., Aarons, J., Reinisch, B., Scali, J., and Kelley, M.: Investigations of thermospheric ionospheric dynamics with 6300-angstrom images from the Arecibo Observatory, J. Geophys. Res., 102, 7331–7343, 1997.

Mukherjee, G. K.: Studies of the equatorial F-region depletions and dynamics using multiple wavelength nightglow imaging, J. Atmos. Solar-Terr. Phys., 65, 379–390, 2003.

Otsuka, Y., Shiokawa, K., Ogawa, T., and Wilkinson, P.: Geomagnetic conjugate observations of equatorial airglow depletions, Geophys. Res. Lett., 29, 1753, doi:10.1029/2002GL015 347, 2002.

Pimenta, A. A., Bittencourt, J. A., Fagundes, P. R., Sahai, Y., Buriti, R. A., Takahashi, H., and Taylor, M. J.: Ionospheric plasma bubble zonal drifts over the tropical region: a study using OI 630 nm emission all-sky images, J. Atmos. Solar-Terr. Phys., 65, 1117–1126, 2003a.

Pimenta, A. A., Fagundes, P. R., Sahai, Y., Bittencourt, J. A., and Abalde, J. R.: Equatorial F-region plasma depletion drifts: latitudinal and seasonal variations, Ann. Geophys., 21, 2315–2322, 2003b.

Sahai, Y., Bittencourt, J. A., Teixeira, N. R., and Takahashi, H.: Simultaneous observations of OI 7774-Å and OI 6300-Å emissions and correlative study with ionospheric parameters, J. Geophys. Res., 86, 3657–3660, 1981a.

Sahai, Y., Bittencourt, J. A., Teixeira, N. R., and Takahashi, H.: Plasma irregularities in the tropical F-region detected by OI 7774 Å and 6300 Å nightglow measurements, J. Geophys. Res., 86, 3496–3500, 1981b.

Sahai, Y., Fagundes, P. R., and Bittencourt, J. A.: Transequatorial F-region ionospheric plasma bubbles: solar cycle effects, J. Atmos. Solar-Terr. Phys., 62, 1377–1383, 2000.

Taylor, M. J., Swenson, G. R., and Taylor, V.: Height measurements of the OI(557.7 nm) gravity wave structure over the Hawaiian-Islands during ALOHA-93, Geophys. Res. Lett., 22, 2881–2884, 1995.

Tinsley, B. A.: Field aligned airglow observations of transequatorial bubbles in the tropical *F*-region, J. Atmos.-Terr. Phys., 44, 547–557, 1982.

Tinsley, B. A. and Bittencourt, J. A.: Determination of *F* region height and peak electron density at night using airglow emissions from atomic oxygen, J. Geophys. Res., 80, 2333–2337, 1975.

Tinsley, B. A., Christensen, A. B., Bittencourt, J., Gouveia, H., Angreji, P. D., and Takahashi, H.: Excitation of Oxygen permitted line emissions in the tropical nightglow, J. Geophys. Res., 78, 1174–1186, 1973.

Tsunoda, R. T.: Control of the seasonal and longitudinal occurrence of equatorial scintillations by the longitudinal gradient in integrated *E* region Pedersen conductivity, J. Geophys. Res., 90, 447–456, 1985.

Weber, E. J., Basu, S., Bullett, T. W., Balladares, C., Bishop, G., Groves, K., Kuenzler, H., Ning, P., Sultan, P. J., Sheehan, R. E., and Araya, J.: Equatorial plasma depletion precursor signatures and onset observed at 11 degrees south of the magnetic equator, J. Geophys. Res., 101, 26 829–26 838, 1996.

Yeh, K. C. and Liu, C. H.: Radio wave scintillations in the ionosphere, Proc. IEEE, 70, 324–360, 1982.

Zalesak, S. T., Ossakow, S. L., and Chaturvedi, P. K.: Nonlinear equatorial spread F: The effect of neutral winds and background Pedersen conductivity, J. Geophys. Res., 87, 151–166, 1982.